



# Multi-physicochemical modeling of direct methane fueled solid oxide fuel cells



Yuanyuan Xie, Hanping Ding, Xingjian Xue\*

Department of Mechanical Engineering, University of South Carolina, 300 Main Street, Room A224, Columbia, SC 29208, USA

## HIGHLIGHTS

- Both  $H_2$ – $H_2O$  and  $CO$ – $CO_2$  electro-oxidation processes are considered in methane SOFC model.
- Elementary reactions are incorporated into the multi-physics processes.
- Comprehensive sensitivity analysis is carried out.
- Mitigation strategy is suggested for surface carbon deposition.

## ARTICLE INFO

### Article history:

Received 8 February 2013

Received in revised form

20 May 2013

Accepted 5 June 2013

Available online 14 June 2013

### Keywords:

Elementary reactions

Carbon deposition

Methane

Modeling

SOFC

## ABSTRACT

Both  $H_2$ – $H_2O$  and  $CO$ – $CO_2$  electro-oxidation processes are considered in direct methane fueled SOFC model and incorporated into the comprehensive couplings between multi bulk transport processes, diffusion processes, surface chemical processes and the cell polarization performance. The model is validated using the experimental data of polarization performance at 600 °C, 650 °C and 700 °C respectively. Upon the model validation, extensive simulations are carried out to elucidate the complicated interaction mechanisms with emphasis on surface reaction processes and surface adsorbates under SOFC operating conditions. Results show that the surface reactions of methane are strongly dependent on the cell operating conditions and increase with increasing the operating temperature and cell current. The bulk gas species and surface adsorbates show different degree of sensitivities to cell operating conditions. Surface carbon deposition can be mitigated through increasing the operating temperature, the cell operating current, and the exchange current of electrodes as well as suitable increasing  $H_2O$  content in the fuel. Surface carbon deposition may also be mitigated through suitable reducing the content of  $CH_4$ ,  $CO$ , and/or  $CO_2$  in the fuel.

Published by Elsevier B.V.

## 1. Introduction

Solid oxide fuel cells (SOFCs) are fuel flexible, which can operate on not only hydrogen but also hydrocarbon fuels [1]. The high temperature operating condition together with hydrocarbon fuel may lead to very complicated reforming and electrochemical oxidation processes within the anode [2]. The recirculation strategy of exhaust gas from the anode to a pre-reformer for further reforming has been employed in many SOFC systems to improve the system efficiency [3–5], these are usually achieved through external reformer. The reforming reactions also occur in porous anode electrode. The fundamental mechanism understanding of reforming process in the anode is very significant, particularly for

direct methane fueled SOFCs. In this respect, mathematical modeling plays an important role as a cost-effective technique.

There are a few modeling studies regarding the direct methane fueled SOFCs [6–9]. One common assumption in these studies is that the chemical reaction processes only take place in bulk gas species, while the adsorbed species on the electrode surface and the corresponding surface reactions are neglected. To overcome these limitations, surface chemical kinetic modeling approach has been developed recently by Bessler et al. [10–13] and Kee et al. [14,15] to describe the detailed surface chemistry. Such models focus on the description of adsorption/desorption and surface reaction processes, and can provide more precise simulations of surface chemical reactions. Toward the better understanding of the interactions between transport processes and surface chemical reactions and their effects on SOFC performance, Janardhanan and Deutschmann [16] presented an isothermal CFD analysis of an anode-supported SOFC button cell, in which the elementary surface

\* Corresponding author. Tel.: +1 803 576 5598; fax: +1 803 777 0106.

E-mail address: [Xue@cec.sc.edu](mailto:Xue@cec.sc.edu) (X. Xue).

reactions were coupled with fluid flow and mass transport processes. Goldin et al. [17] studied a multidimensional non-isothermal modeling of hydrocarbon fueled SOFC button cell with relatively comprehensive coupling between bulk transport processes and surface chemistry, in which the effects of different operating conditions on the cell performance were investigated. All of these researches represent significant progresses toward the modeling of hydrocarbon-fueled SOFCs.

Built upon the above progresses of SOFC modeling in open literature, the objective of this research is to develop a direct methane fueled SOFC model toward the understanding of fundamental mechanisms within SOFCs particularly the porous anode. The model takes into account both  $H_2$ – $H_2O$  and  $CO$ – $CO_2$  electro-oxidation processes and incorporates these two electro-oxidation processes into the complicated coupling between bulk transport processes, diffusion processes, and surface chemical processes. A button cell test system is used as the physical base for the model development and the corresponding experimental data is utilized to validate the model. Upon the model validation, extensive simulations are performed to elucidate the complicated interactions between transport processes and surface reactions as well as their effects on the cell performance with emphasis on surface reaction processes under practical button cell operating conditions. The different roles and relative importance of various surface chemical kinetic and electro-oxidation processes are studied through sensitivity analysis. The carbon deposition issue is also studied through the analysis of adsorbed surface carbons and the potential mitigation strategies are suggested.

## 2. Experimental and model setup

Fig. 1 shows a schematic illustration of the experimental setup. An anode-supported Ni–YSZ/YSZ/YSZ–LSM button cell is mounted on the top of a vertical ceramic tube. The humidified methane is supplied to the anode electrode via a small ceramic tube located at the center of the large vertical tube, and the surplus gas and reaction products flow out from the large tube. The cathode electrode is exposed to the ambient air. A furnace is utilized to control the temperature of the cell test stand. Such an experimental test system

is used to obtain the polarization performance of the button cell under different operating conditions and is employed as a physical base for mathematical model development. Due to the axial-symmetry, a two-dimensional axial-symmetric computational domain is considered to model the button cell test system.

## 3. Mathematical model

### 3.1. Heterogeneous surface chemistry in electrodes

The heterogeneous chemical/electrochemical processes are influenced by not only the applied materials and catalysts but also the heterogeneous distribution of fuel species. The processes are much more complicated with hydrocarbon fuels than those with hydrogen fuel. For methane fueled Ni–YSZ/YSZ/YSZ–LSM button cell, the total of 21 reversible elementary reactions could occur with nickel as the anode catalysis [18] and is summarized in Table 1. The processes describe the basic mechanisms of methane reforming processes including dissociation, steam reforming, dry reforming and water–gas-shift process [19,20]. These elementary reactions consist of two types of processes: the adsorption/desorption processes and surface reaction processes. The surface of Ni provides the interaction site among adsorbed species without involving the electrochemical reactions and charge transfer processes [21]. At Ni–YSZ–gas triple phase boundary, charge transfer reactions take place between the adsorbed species and oxygen ions conducted from the electrolyte layer. The identification of kinetic steps of charge transfer is still difficult from experiments. It is envisioned that many charge transfer pathways may exist simultaneously [10,12,13], but only a few of them are rate-dominating steps. Therefore, in our following modeling, the  $H_2$ – $H_2O$  and  $CO$ – $CO_2$  electro-oxidation pathways are assumed to be the two dominant electrochemical processes.

At equilibrium state the net current density is zero, but the reaction rates in the anode and cathode are not zero. As a result, the equilibrium overpotential is built. Specifically for the hydrogen oxidation process, the local equilibrium potential can be determined by,

$$\eta_{H_2} = \frac{\Delta G}{zF} + \frac{RT}{2F} \ln \left( \frac{p_{H_2} p_{O_2}^{0.5}}{p_{H_2O}} \right) \quad (1)$$

where  $\Delta G$  is the Gibbs free energy of the reaction,  $z$  is the number of electrons,  $p$  is the partial pressure. And the local Butler–Volmer equation can be formulated as,

$$i_{an}^{H_2} = z \cdot F \cdot l_{TPB} \cdot i_{0,an}^{H_2} \left[ \exp \left( \frac{\alpha z F}{RT} (\eta - \eta_{H_2}) \right) - \exp \left( - \frac{(1 - \alpha) z F}{RT} (\eta - \eta_{H_2}) \right) \right] \quad (2)$$

where  $l_{TPB}$  is the three phase boundary length per unit volume,  $i_{0,an}^{H_2}$  is the exchange current density and can be formulated as [15],

$$i_{0,an}^{H_2} = i_{H_2}^* \frac{(p_{H_2}/p_{H_2}^*)^{0.25} (p_{H_2O})^{0.75}}{1 + (p_{H_2}/p_{H_2}^*)^{0.5}} \quad (3)$$

where  $p_{H_2}^*$  is about 0.7 atm;  $i_{H_2}^*$  is the empirical constant used to fit the numerical results with experimental data.

The carbon monoxide oxidation process is quite similar to that of hydrogen [22]. It has been realized that the rate of CO oxidation is about 2–3 times less than that of hydrogen oxidation under the same oxidant partial pressure [23]. When the rate of CO oxidation

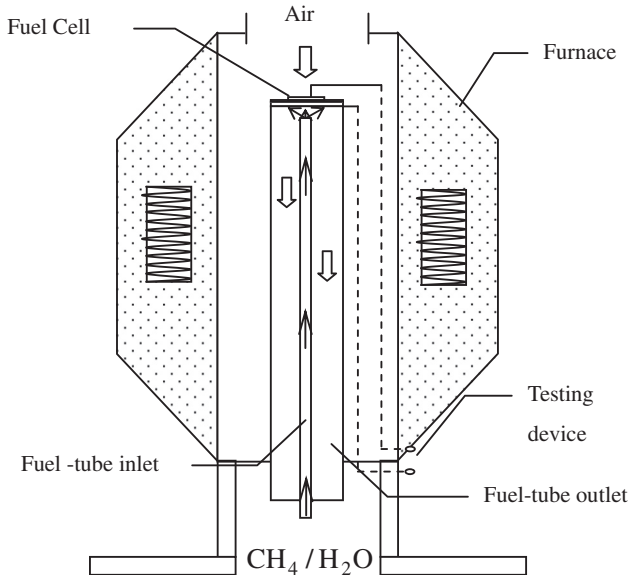


Fig. 1. Schematic illustration of button cell test system.

**Table 1**  
Surface reaction mechanism of methane.

Anode surface (Ni/YSZ)		A	n	E
<i>Adsorption/desorption (f/b)</i>				
1	$\text{H}_2 + \text{Ni(s)} + \text{Ni(s)} \rightleftharpoons \text{H(s)} + \text{H(s)}$	$10^{-2}; 5.593 \times 10^{19}$	0;0	0; 88.12
2	$\text{O}_2 + \text{Ni(s)} + \text{Ni(s)} \rightleftharpoons \text{O(s)} + \text{O(s)}$	$10^{-2}; 2.508 \times 10^{23}$	0;0	0; 470.39
3	$\text{CH}_4 + \text{Ni(s)} \rightleftharpoons \text{CH}_4(\text{s})$	$8 \times 10^{-3}; 5.302 \times 10^{15}$	0;0	0; 33.15
4	$\text{H}_2\text{O} + \text{Ni(s)} \rightleftharpoons \text{H}_2\text{O(s)}$	$1 \times 10^{-1}; 4.579 \times 10^{12}$	0;0	0; 62.68
5	$\text{CO}_2 + \text{Ni(s)} \rightleftharpoons \text{CO}_2(\text{s})$	$1 \times 10^{-5}; 9.334 \times 10^7$	0;0	0; 28.80
6	$\text{CO} + \text{Ni(s)} \rightleftharpoons \text{CO(s)}$	$5 \times 10^{-1}; 4.041 \times 10^{11}$	0;0	0; 112.85
<i>Surface reactions</i>				
7	$\text{O(s)} + \text{H(s)} \rightleftharpoons \text{OH(s)} + \text{Ni(s)}$	$5 \times 10^{22}; 2.005 \times 10^{21}$	0;0	97.9; 37.19
8	$\text{OH(s)} + \text{H(s)} \rightleftharpoons \text{H}_2\text{O(s)} + \text{Ni(s)}$	$3 \times 10^{20}; 2.175 \times 10^{21}$	0;0	42.7; 91.36
9	$\text{OH(s)} + \text{OH(s)} \rightleftharpoons \text{O(s)} + \text{H}_2\text{O(s)}$	$3 \times 10^{21}; 5.423 \times 10^{23}$	0;0	100; 209.37
10	$\text{O(s)} + \text{C(s)} \rightleftharpoons \text{CO(s)} + \text{Ni(s)}$	$5.2 \times 10^{23}; 1.418 \times 10^{22}$	0;−3	148.1; 115.97
11	$\text{O(s)} + \text{CO(s)} \rightleftharpoons \text{CO}_2(\text{s}) + \text{Ni(s)}$	$2 \times 10^{19}; 3.214 \times 10^{23}$	0;−1	123.6; 86.5
12	$\text{HCO(s)} + \text{Ni(s)} \rightleftharpoons \text{CO(s)} + \text{H(s)}$	$3.7 \times 10^{21}; 2.338 \times 10^{20}$	0;−1	0; 127.98
13	$\text{HCO(s)} + \text{Ni(s)} \rightleftharpoons \text{O(s)} + \text{CH(s)}$	$3.7 \times 10^{24}; 7.914 \times 10^{20}$	−3;0	95.8; 114.22
14	$\text{CH}_4(\text{s}) + \text{Ni(s)} \rightleftharpoons \text{CH}_3(\text{s}) + \text{H(s)}$	$3.7 \times 10^{21}; 4.438 \times 10^{21}$	0;0	57.7; 58.83
15	$\text{CH}_3(\text{s}) + \text{Ni(s)} \rightleftharpoons \text{CH}_2(\text{s}) + \text{H(s)}$	$3.7 \times 10^{24}; 9.513 \times 10^{22}$	0;0	100; 52.58
16	$\text{CH}_2(\text{s}) + \text{Ni(s)} \rightleftharpoons \text{CH(s)} + \text{H(s)}$	$3.7 \times 10^{24}; 3.008 \times 10^{24}$	0;0	97.1; 76.43
17	$\text{CH(s)} + \text{Ni(s)} \rightleftharpoons \text{C(s)} + \text{H(s)}$	$3.7 \times 10^{21}; 4.4 \times 10^{22}$	0;0	18.8; 160.49
18	$\text{CH}_4(\text{s}) + \text{O(s)} \rightleftharpoons \text{CH}_3(\text{s}) + \text{OH(s)}$	$1.7 \times 10^{24}; 8.178 \times 10^{22}$	0;0	88.3; 28.72
19	$\text{CH}_3(\text{s}) + \text{O(s)} \rightleftharpoons \text{CH}_2(\text{s}) + \text{OH(s)}$	$3.7 \times 10^{24}; 3.815 \times 10^{21}$	0;0	130.1; 21.97
20	$\text{CH}_2(\text{s}) + \text{O(s)} \rightleftharpoons \text{CH(s)} + \text{OH(s)}$	$3.7 \times 10^{24}; 1.206 \times 10^{23}$	0;0	126.8; 45.42
21	$\text{CH(s)} + \text{O(s)} \rightleftharpoons \text{C(s)} + \text{OH(s)}$	$3.7 \times 10^{21}; 1.764 \times 10^{21}$	0;0	48.1; 129.08
<i>Charge transfer reactions (TPB)</i>		<i>Global B–V equation</i>		
22	$\text{H(s)} + \text{O}^{2-}(\text{YSZ}) \rightleftharpoons \text{OH}^-(\text{s}) + \text{e}^-(\text{Ni})$	$i_{\text{an}}^{\text{H}_2} = zF l_{\text{TPB}} i_{0,\text{an}}^{\text{H}_2} \left[ \exp\left(\frac{\alpha z F}{RT}(\eta - \eta_{\text{H}_2})\right) - \exp\left(-\frac{(1-\alpha)z F}{RT}(\eta - \eta_{\text{H}_2})\right) \right]$		
23	$\text{H(s)} + \text{OH}^-(\text{YSZ}) \rightleftharpoons \text{H}_2\text{O(s)} + \text{e}^-(\text{Ni})$	$i_{\text{an}}^{\text{CO}} = \frac{1}{3} zF l_{\text{TPB}} i_{0,\text{an}}^{\text{CO}} \left[ \exp\left(\frac{\alpha z F}{RT}(\eta - \eta_{\text{CO}})\right) - \exp\left(-\frac{(1-\alpha)z F}{RT}(\eta - \eta_{\text{CO}})\right) \right]$		
24	$\text{C(s)} + \text{O}^{2-}(\text{YSZ}) \rightleftharpoons \text{CO(s)} + 2\text{e}^-(\text{Ni})$	$i_{\text{an}} = i_{\text{an}}^{\text{H}_2} + i_{\text{an}}^{\text{CO}}$		
25	$\text{CO(s)} + \text{O}^{2-}(\text{YSZ}) \rightleftharpoons \text{CO}_2(\text{s}) + 2\text{e}^-(\text{Ni})$			
<i>Electrolyte (YSZ)</i>				
26	$\text{O}_0^*(\text{YSZ}) + (\text{YSZ}) \rightleftharpoons \text{O}_0^*(\text{YSZ}) + \text{V}_0^*(\text{YSZ})$			
<i>Cathode surface (LSM)</i>		$A^0$	$\alpha$	$E$
27	$\text{O}_2(\text{g}) + 2(\text{LSM}) \rightleftharpoons 2\text{O}(\text{LSM})$	$10^{-2}; 2.3 \times 10^{15}$	0	0;258.2
28	$\text{O}(\text{LSM}) + \text{V}_0^*(\text{YSZ}) + 2\text{e}^- \rightleftharpoons \text{O}_0^*(\text{YSZ}) + (\text{LSM})$	$i_{\text{ca}} = zF l_{\text{TPB}} i_{0,\text{ca}} \left[ \exp\left(\frac{\alpha z F}{RT}(\eta - \eta_{\text{eq}})\right) - \exp\left(-\frac{(1-\alpha)z F}{RT}(\eta - \eta_{\text{eq}})\right) \right]$		

Rate constant of Arrhenius equation written as:  $k = AT^m \exp(-E/RT)$ , the unit of  $E$  is kJ/mol.

reaction is assumed to be three times lower than that of  $\text{H}_2$  oxidation, the modeling result is able to obtain a good agreement with experimental data [24]. Therefore, this assumption is employed to describe  $\text{CO}-\text{CO}_2$  oxidation reaction,

$$\eta_{\text{CO}} = \frac{\Delta G}{zF} + \frac{RT}{2F} \ln \left( \frac{p_{\text{CO}} p_{\text{O}_2}^{0.5}}{p_{\text{CO}_2}} \right) \quad (4)$$

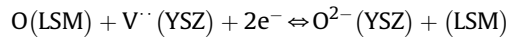
$$i_{\text{an}}^{\text{CO}} = \frac{1}{3} z \cdot F \cdot l_{\text{TPB}} \cdot i_{0,\text{an}}^{\text{CO}} \left[ \exp\left(\frac{\alpha z F}{RT}(\eta - \eta_{\text{CO}})\right) - \exp\left(-\frac{(1-\alpha)z F}{RT}(\eta - \eta_{\text{CO}})\right) \right] \quad (5)$$

$$i_{0,\text{an}}^{\text{CO}} = i_{\text{CO}}^* \frac{(p_{\text{CO}}/p_{\text{CO}}^*)^{0.25} (p_{\text{CO}_2})^{0.75}}{1 + (p_{\text{CO}}/p_{\text{CO}}^*)^{0.5}} \quad (6)$$

where  $i_{\text{CO}}^*$  is the empirical constant. Then, the total exchange current density within the anode can be formulated as,

$$i_{\text{an}} = i_{\text{an}}^{\text{H}_2} + i_{\text{an}}^{\text{CO}} \quad (7)$$

At the cathode side, two-step oxygen reduction reaction is assumed in order to keep the consistence of electrochemical reaction and charge transfer process:



and the global Butler–Volmer equation can be built by,

$$i_{\text{ca}} = z \cdot F \cdot l_{\text{TPB}} \cdot i_{0,\text{ca}} \left[ \exp\left(\frac{\alpha z F}{RT}(\eta - \eta_{\text{eq}})\right) - \exp\left(-\frac{(1-\alpha)z F}{RT}(\eta - \eta_{\text{eq}})\right) \right] \quad (8)$$

$$i_{0,\text{ca}} = i_{\text{O}_2}^* \frac{(p_{\text{O}_2}/p_{\text{O}_2}^*)^{0.25}}{1 + (p_{\text{O}_2}/p_{\text{O}_2}^*)^{0.5}} \quad (9)$$

where  $p_{\text{O}_2}^* = 4.9 \times 10^8 \exp(-2 \times 10^5/RT)$ ;  $i_{\text{O}_2}^*$  is the empirical fitting parameter;  $\eta_{\text{eq}}$  is the equilibrium overpotential (e.g.,  $\eta_{\text{eq}} = 0.75\eta_{\text{H}_2} + 0.25\eta_{\text{CO}}$ ).

### 3.2. Surface diffusion

According to the mean field approach [19], the concentration of surface species  $i$  can be normalized by the total available surface sites  $\Gamma$ , yielding the surface coverage ( $\theta = c_i \sigma_i^{\text{surf}}/\Gamma$ ), a

**Table 2**  
Governing equations.

Charge	$-\nabla \cdot (\sigma_n^{\text{eff}} \nabla V_n) = \pm i_r, \quad n = e, i$ $\sigma_e^{\text{eff}} = \phi \left( \frac{1-\epsilon}{\tau} \right) \sigma_e, \quad \sigma_i^{\text{eff}} = (1-\phi) \left( \frac{1-\epsilon}{\tau} \right) \sigma_i$
Mass	$\nabla \cdot J_m + \rho v \cdot \nabla w_m = R_m,$ $J_m = -\rho w_m \sum_k D_{m,k}^{\text{eff}} \left[ \nabla x_k + (x_k - w_k) \frac{\nabla p}{p} \right],$ $D_{m,k}^{\text{eff}} = \left( \frac{\tau}{\epsilon D_{m,k}} + \frac{1}{D_{kn}} \right)^{-1},$ $D_{m,k} = 10^{-3} \frac{T^{1.75} (1/M_m + 1/M_k)^{0.5}}{p \left[ (\sum_l v_{ml})^{1/3} + (\sum_l v_{kl})^{1/3} \right]^2},$ $D_{kn} = \frac{d_{nc}}{2} \sqrt{\frac{8\epsilon NT}{\pi M}}$
Momentum	$\nabla p + \rho(v \cdot \nabla)v = \nabla \cdot \left[ \mu(\nabla v + (\nabla v)^T) - \frac{2}{3} \mu(\nabla \cdot v)I \right]$ $\nabla \cdot (p v) = 0,$ $\frac{\mu}{R} v = -\nabla p + \frac{1}{\epsilon} \nabla \cdot \left\{ \mu \left[ \nabla v + (\nabla v)^T \right] - \frac{2}{3} \mu(\nabla \cdot v)I \right\},$ $K = \frac{\epsilon^3 d_p^2}{150(1-\epsilon)^2}$
Heat	$c_p v \cdot \nabla T - \nabla \cdot (k_e \nabla T) = Q_h,$ $k_e = \beta k_l + (1-\beta)k_s,$ $Q_{h,r} = r \cdot \Delta H, \quad Q_{h,ac} = -(\eta_{\text{act}} + \eta_{\text{con}}) \cdot i \cdot A V_e, \quad Q_{h,ohm} = i^2 / \sigma$

dimensionless parameter. As a result, the surface diffusion process can be described by [12],

$$\frac{\sigma_i^{\text{surf}}}{\Gamma} R_n = -\nabla \cdot \left( D_i^{\text{surf}} \nabla \theta_i \right) \quad (10)$$

where  $\sigma_i^{\text{surf}}$  is the number of surface sites occupied by species  $i$ ;  $D_i^{\text{surf}}$  is the surface diffusivity of species  $i$  ( $D_i^{\text{surf}} = D_i^0 \exp(-E_i^{\text{act}}/RT)$ );  $R_n$  is the net reaction rate for species  $n$  and can be determined as,

$$R_n = \sum_n v_n \left( k_f \prod_i [c_i^{\text{Ra}}]^{n_i} - k_b \prod_j [c_j^{\text{Pu}}]^{m_j} \right) \quad (11)$$

where  $v_n$  is the pre-factor for elementary reaction;  $c_i^{\text{Ra}}$  and  $c_j^{\text{Pu}}$  are the concentrations of reactant and product respectively while  $n_i$  and  $m_j$  are the corresponding stoichiometric factors;  $k_f$ ,  $k_b$  are the forward and backward reaction rates respectively, and can be described by the Arrhenius expression [11],

$$k_f = A T^n \exp\left(\frac{-E_f^{\text{act}}}{RT}\right), \quad k_b = A T^n \exp\left(\frac{-E_b^{\text{act}}}{RT}\right) \quad (12)$$

here  $A$ ,  $n$  and  $E^{\text{act}}$  are the Arrhenius parameters, their values can be found in Table 1 for each of the individual reactions.

**Table 3**  
Reaction rates and source terms.

Net reaction rate of adsorbates	Reaction source term	Energy source term
$r_{\text{CH4(s)}} = r_3 - r_{14} - r_{18}$	$R_{\text{H2}} = -2r_1$	$R_{\text{Ca}} = Q_{\text{ohm}} + Q_{\text{chem}}$
$r_{\text{CH3(s)}} = r_{14} - r_{15} + r_{18} - r_{19}$	$R_{\text{CH4}} = -r_2$	$R_{\text{El}} = Q_{\text{ohm}}$
$r_{\text{CH2(s)}} = r_{15} - r_{16} + r_{19} - r_{20}$	$R_{\text{H2O}} = -r_4$	$R_{\text{An}} = Q_{\text{ohm}} + Q_{\text{chem}}$
$r_{\text{CH(s)}} = r_{16} - r_{17} + r_{20} - r_{21}$	$R_{\text{CO2}} = -r_5$	$R_{\text{Cl}} = 0$
$r_{\text{C(s)}} = -r_{10} + r_{17} + r_{21} - r_{24}$	$R_{\text{CO}} = -r_6$	
$r_{\text{CO(s)}} = r_6 + r_{10} - r_{11} + r_{12} + r_{24} - r_{25}$	$R_{\text{O2}} = -r_{27}$	
$r_{\text{CO2(s)}} = r_5 + r_{11} + r_{25}$		
$r_{\text{H(s)}} = 2r_1 - r_7 - r_8 + r_{12} + r_{14} + r_{15} + r_{16} + r_{17} - r_{22} - r_{23}$		
$r_{\text{OH(s)}} = r_7 - r_8 - r_9 + r_{13} + r_{18} + r_{19} + r_{20} + r_{21} + r_{22} - r_{23}$		
$r_{\text{O(LSM)}} = 2r_{27} - r_{18}$		

### 3.3. Transport processes within the cell

In addition to the surface chemistry and electro-oxidation processes, SOFCs also include very complicated transport processes, such as fuel/gas transport in fuel supply tubes and porous electrodes, charge transport through material backbone, as well as heat transfer. The mass and charge transport processes are coupled together at reaction sites of porous electrodes through elementary reactions mentioned above. To elucidate these complicated transport and reaction mechanisms, the governing equations for multi-transport processes are summarized in Table 2, the detailed modeling approach can be found in our previous study [25]. The applied operating parameters and corresponding boundary conditions are listed in Tables 3–5 respectively. In the model, several assumptions are employed: (1) the catalyst Ni is uniformly distributed within the anode electrode; (2) the microstructure of electrodes is homogeneous and stable; and (3) the effects of carbon deposition on the pore structure and catalytic activity of Ni are neglected.

## 4. Solution algorithm and model validation

The mathematical model is solved using COMSOL MULTIPHYSICS V4.0. For a specified cell voltage at the cathode electrode boundary, the corresponding average cell current density and the species distributions are calculated. The cell polarization curve is then obtained by specifying a series of cell voltages and calculating the corresponding average cell current density. The species distributions associated with multi-physics transport and surface reaction processes are calculated at each of the individual voltage conditions.

The model is validated using experimental polarization curves, where the mixture of 97% CH<sub>4</sub> + 3% H<sub>2</sub>O is used as the fuel and ambient oxygen as the oxidant. The cell polarization curve is obtained at three temperatures of 600 °C, 650 °C and 700 °C respectively. As shown in Fig. 2, the model predictions match with experimental data reasonably well. This model is then used for further numerical studies.

## 5. Results and discussion

### 5.1. Distribution of gas species and adsorbates

Fig. 3 shows the distributions of gas species within the fuel supply tubes and the porous anode. Here the operating temperature for the simulation is 700 °C and the cell voltage is set at 0.5 V as an example. Within the small fuel supply tube, the distributions of gas species are relatively uniform. Beyond the outlet of the small tube, the molar fractions of CH<sub>4</sub> and CO decrease toward the anode electrode and increase from the anode electrode toward the outlet

**Table 4**  
Operation parameters.

	Value	Units
Cathode layer thickness, radius	$4 \times 10^{-5}, 2.5 \times 10^{-3}$	m
Electrolyte layer thickness, radius	$2 \times 10^{-5}, 6.5 \times 10^{-3}$	m
Anode layer thickness, radius	$3.5 \times 10^{-4}, 6.5 \times 10^{-3}$	m
Inlet fuel channel radius, wall radius	$1 \times 10^{-3}, 1.5 \times 10^{-3}$	m
Outlet fuel channel radius	$6.5 \times 10^{-3}$	m
Gas constant	8.314	J mol <sup>-1</sup> K <sup>-1</sup>
Pressure	1	atm
Anode ionic conductivity	$3.34 \times 10^4 \exp(-10,300/T)$	Sm <sup>-1</sup>
Cathode ionic conductivity	$3.34 \times 10^4 \exp(-10,300/T)$	Sm <sup>-1</sup>
Anode electronic conductivity	$2 \times 10^6$	Sm <sup>-1</sup>
Cathode electronic conductivity	$42 \times 10^6 \exp(-1150/T)/T$	Sm <sup>-1</sup>
Electrolyte ionic conductivity	$3.34 \times 10^4 \exp(-10,300/T)$	Sm <sup>-1</sup>
Porosity ( $\epsilon$ )	0.4	1
Particle diameter	$2 \times 10^{-6}$	m
Tortuosity	$((3 - \epsilon)/2)^{0.5}$	1
Permeability	$\epsilon^3 d^2 / (1 - \epsilon)^2 / 150$	1
Inlet velocity	0.2	ms <sup>-1</sup>
Surface site density of Ni	$6.1 \times 10^{-9}$	mol cm <sup>-2</sup>
Specific three-phase boundary length	$1.8 \times 10^{12}$	m m <sup>-3</sup>

of the large ceramic tube. The molar fractions show relatively large gradients near the porous anode. The molar fractions of H<sub>2</sub>O and CO<sub>2</sub> show opposite trends. Essentially, the surface reactions in the anode consume adsorbed hydrocarbon fuel CH<sub>4</sub>, and generate H<sub>2</sub>O and CO<sub>2</sub> through the electrochemical reaction processes. The CO species is generated through surface reaction process and consumed by oxidation process. The combinational effects lead to the species distributions mentioned above.

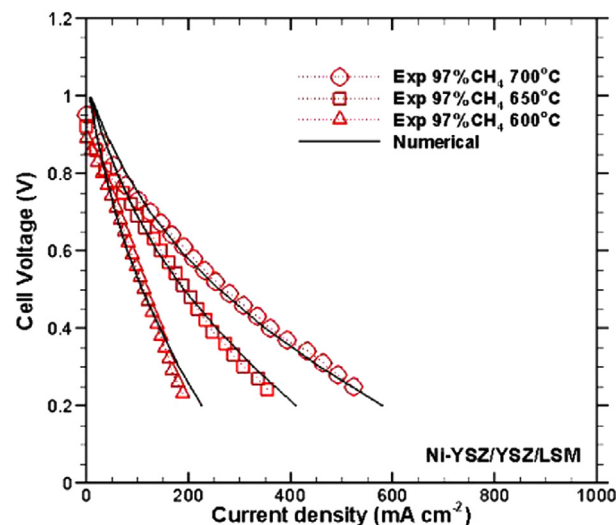
Fig. 4 illustrates the major adsorbed species on the anode porous electrode surface, which are important reaction intermediates affecting the CH<sub>4</sub> conversion and oxidation processes. The surface coverage of all surface adsorbed intermediates, e.g., CH<sub>4</sub>(s), CH<sub>3</sub>(s), CH<sub>2</sub>(s), CH(s), C(s) and H(s) decrease from the channel/anode interface and anode circumference toward the anode/electrolyte interface, while the surface oxidation products of H<sub>2</sub>O(s) and CO<sub>2</sub>(s) shows opposite trend, decreasing from the anode/electrolyte interface toward the channel/anode interface and anode circumference. These observations indicate that the surface reactions of methane and electro-oxidation processes are relatively intensive near the anode/electrolyte interface. As mentioned above, for Ni-based anode, the hydrocarbon fuel could lead to the deposition of carbon on the surface of catalyst Ni, resulting in the deactivation of Ni catalytic function. As shown in Fig. 4, the surface coverage of adsorbed carbon is relatively high at the circumference of the anode and decreases toward the electrolyte/anode interface. Since the electrochemical reactions are relatively intensive near the electrolyte/anode interface and relatively weak at the circumference of the anode, it seems that the strong electrochemical reactions may facilitate to mitigate carbon adsorptions.

### 5.2. Local ionic/electronic potential and current

The distributions of local ionic/electronic potential and current densities are shown in Fig. 5. It can be seen that the electronic potential in the cathode maintains at the specified level of 0.5 V

**Table 5**  
Boundary conditions.

Interfaces ( $\Omega$ )	$\Omega_{Ca/Cl}$	$\Omega_{Ca/El}$	$\Omega_{El/An}$	$\Omega_{An/Cl}$	$\Omega_{Cl}$
Ionic charge	Insulation	Continuity	Continuity	Insulation	N/A
Electronic charge	Specified voltage	Insulation	Insulation	0	N/A
Mass	O <sub>2</sub> /N <sub>2</sub> (mass fractions)	Insulation	Insulation	Continuity	CH <sub>4</sub> /H <sub>2</sub> O (mass fraction)
Momentum	Pressure	Wall (no slip)	Wall (no slip)	Continuity	Flow rate, pressure
Energy	Temperature	Continuity	Continuity	Continuity	Temperature

**Fig. 2.** Comparisons between model predictions and experimental data.

while that in the anode is approximately equal to zero. The electronic current density decreases from the channel/anode interface toward the anode/electrolyte interface. The ionic potential decreases from the channel/anode interface toward the anode/electrolyte interface as well as from the anode circumference to the axial-symmetric line of the anode. The corresponding ionic current density distribution shows opposite trend. Since the YSZ electrolyte layer only allows oxygen ions to migrate through, the highest ionic current density around the anode/electrolyte layer indicates that the electrochemical reactions are much intensive at this site.

### 5.3. Effect of operating temperature and current

The operating temperature/current can significantly affect multi-physics transport processes. This issue has been studied extensively in open literature. Usually the distributions of gas species are calculated under different temperature/current conditions and the corresponding SOFC performance is interpreted based on the bulk species distributions. However, it is rare in open literature to extensively study the distributions of adsorbed surface species under such operating conditions because of lacking of coherent links between bulk transport processes and surface reaction processes in SOFC button cell modeling. With the model developed in this paper, we are able to determine various surface species distributions under practical button cell operating conditions. Since the bulk species distributions have been investigated extensively in open literature, here we focus on adsorbed surface species in this paper, the bulk species distributions will not be shown for the concise and compact descriptions.

To examine the temperature effects on the surface chemistry, the distributions of surface adsorbed species along the axis-symmetrical line of the button cell are obtained under three



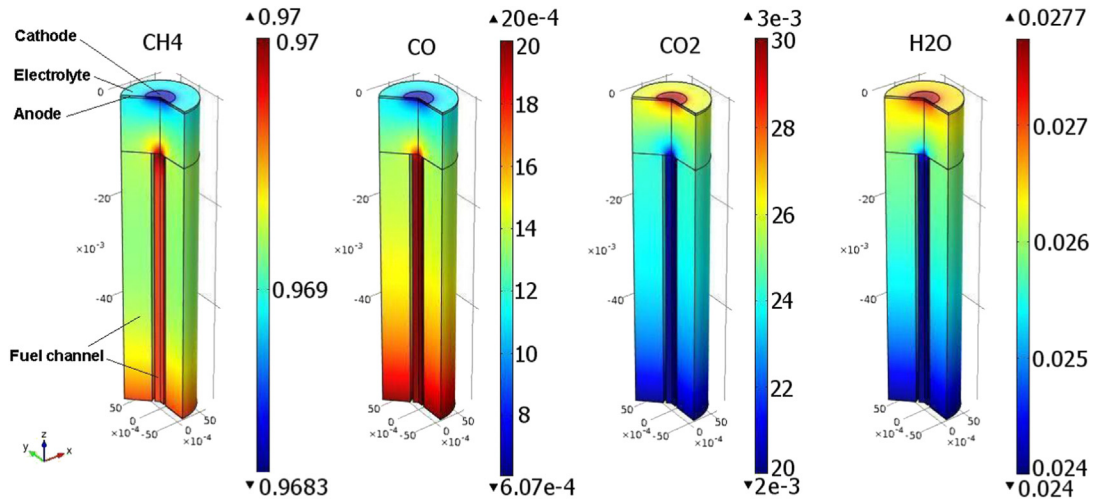


Fig. 3. Distributions of fuel/gas species within fuel supply tubes and anode electrode.

temperatures of 600 °C, 650 °C and 700 °C respectively. Here the cell voltage is set at 0.5 V as an example. As shown in Fig. 6, the surface coverage of adsorbed  $\text{CH}_4(\text{s})$ ,  $\text{CH}_3(\text{s})$ ,  $\text{CH}_2(\text{s})$ ,  $\text{CH}(\text{s})$ , and  $\text{H}_2\text{O}(\text{s})$  are pretty uniform and those of adsorbed  $\text{CO}(\text{s})$ ,  $\text{H}(\text{s})$ , and  $\text{C}(\text{s})$  decrease from the anode/electrolyte interface toward the

channel/anode interface along this axis-symmetrical line. The surface coverage of all these adsorbates decreases with increasing the operating temperature. It is worth noting that the surface coverage of carbon significantly decreases particularly near the anode/electrolyte interface when the temperature increases from 600 °C to

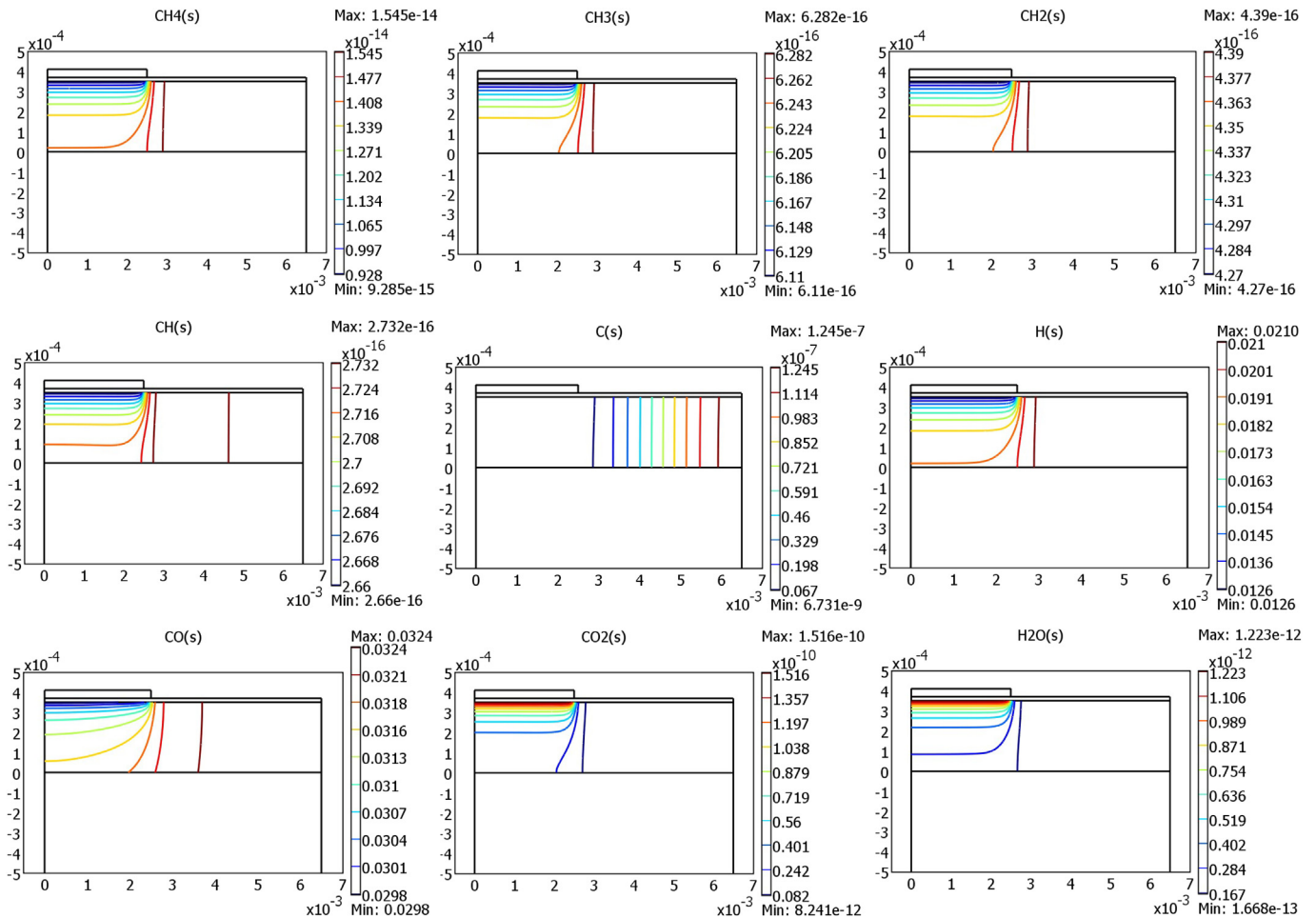


Fig. 4. Distributions of surface coverage of adsorbed species within anode electrode.

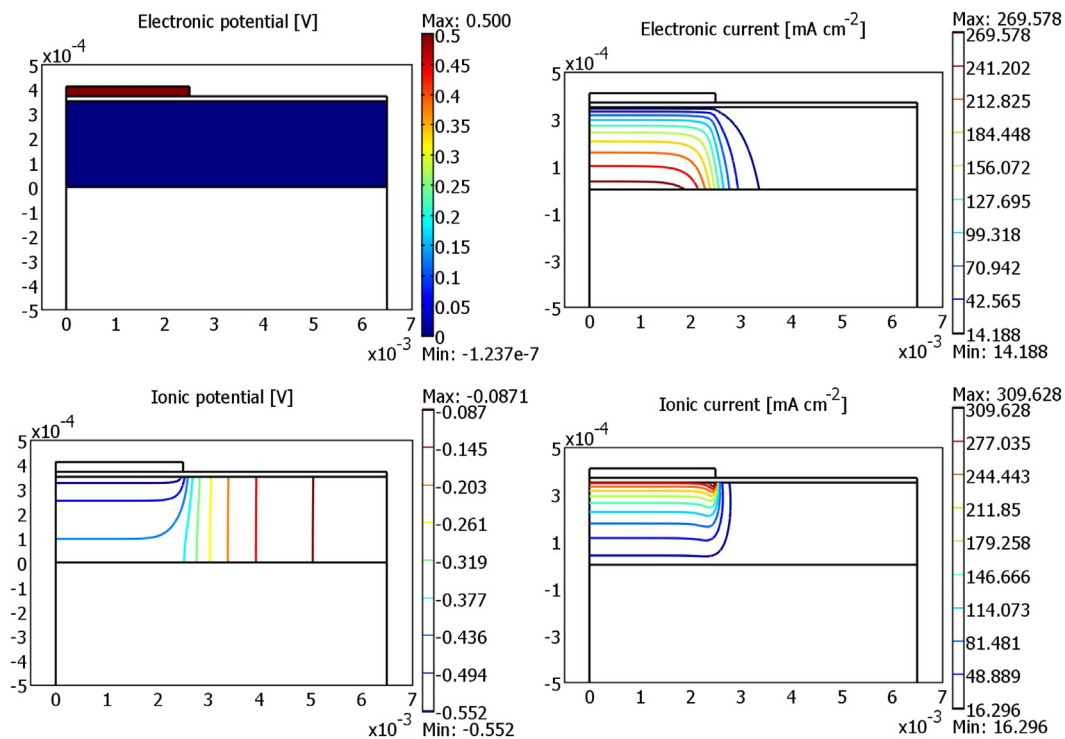


Fig. 5. Distributions of electronic/ionic potential and current density within the anode.

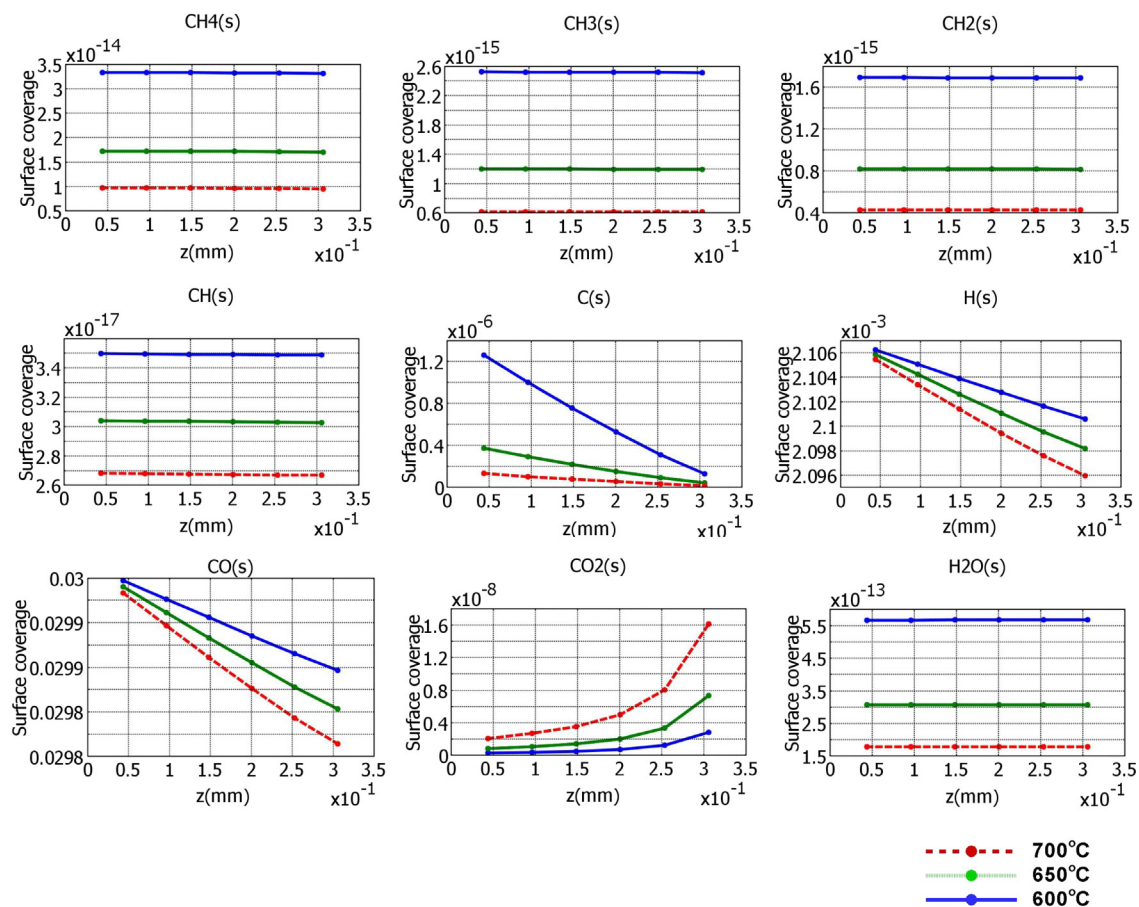


Fig. 6. Distributions of adsorbed species along the axis-symmetrical line of the cell under different operating temperatures.

700 °C, indicating that high operating temperature may potentially mitigate the surface carbon deposition. The surface coverage of adsorbed  $\text{CO}_2(\text{s})$  increases nonlinearly from the anode/electrolyte interface toward the channel/anode interface along the axis-symmetrical line and increase with raising the operating temperatures.

The effects of the cell current on the surface adsorbed species are shown in Fig. 7. The surface coverage of methane dissociation intermediates, e.g.,  $\text{CH}_4(\text{s})$ ,  $\text{CH}_3(\text{s})$ ,  $\text{CH}_2(\text{s})$ ,  $\text{CH}(\text{s})$ , and  $\text{H}(\text{s})$  and  $\text{CO}(\text{s})$  decreases with increasing the cell current density, while that of  $\text{H}_2\text{O}(\text{s})$  and  $\text{CO}_2(\text{s})$  increases. Since the intermediate species  $\text{CH}_4(\text{s})$ ,  $\text{CH}_3(\text{s})$ ,  $\text{CH}_2(\text{s})$ ,  $\text{CH}(\text{s})$ , and  $\text{H}(\text{s})$  and  $\text{CO}(\text{s})$  are consumed and those of  $\text{H}_2\text{O}(\text{s})$  and  $\text{CO}_2(\text{s})$  are generated, increasing the current density improves the forward electrochemical reactions, consuming more fuels while generating more products. It is interesting to note that the adsorbed carbon  $\text{C}(\text{s})$  decreases with increasing the current density, implying that high current density inhibits carbon deposition on the surface of catalyst Ni. Increasing the current improves the  $\text{O}^{2-}$  ions conducting from the cathode to anode side and the generation of more  $\text{O}(\text{s})$  ions on the anode surface, as a result, enhancing oxidation reaction of adsorbed carbon  $\text{C}(\text{s})$ .

#### 5.4. Sensitivity analysis of bulk gas species

The surface elementary reaction processes are very complicated when hydrocarbon, e.g., methane, is used as the fuel. To study the different roles and relative importance of different processes and associated surface intermediates, the sensitivity analysis is carried out. Here the operating temperature is 700 °C and the cell voltage is set at 0.5 V.

In the first case study, the sensitivities of the bulk gas species and adsorbates with respect to the variation of the supplied  $\text{CH}_4$  are studied. The simulations are run by adding 10% more methane to the anode inlet. Fig. 8 shows the corresponding variations of various species at the intersect point between the anode/electrolyte interface and the cell axial-symmetric line. It is clearly seen that the surface adsorbed species carbon  $\text{C}(\text{s})$  is very sensitive to the change of the supplied methane. Here  $\text{C}(\text{s})$  increases significantly with increasing the methane fraction in the fuel. The bulk gas species  $\text{CO}_2$  and the surface adsorbed species  $\text{H}_2\text{O}(\text{s})$ ,  $\text{CH}_4(\text{s})$ ,  $\text{CH}_3(\text{s})$ ,  $\text{CH}_2(\text{s})$ ,  $\text{CH}(\text{s})$ , and  $\text{H}(\text{s})$  show different degree of sensitivities to the variation of the supplied methane. The rest of species are not sensitive to the supplied methane. Similarly by adding 10% more  $\text{H}_2\text{O}$  to the anode inlet and running the simulation, the sensitivities of the bulk gas species and surface adsorbates relative to the variation of the supplied  $\text{H}_2\text{O}$  can be obtained. As shown in Fig. 8, increasing the  $\text{H}_2\text{O}$  content in the anode actually improves the contents of  $\text{CH}_4(\text{s})$ ,  $\text{CH}_3(\text{s})$ ,  $\text{CH}_2(\text{s})$ ,  $\text{CH}(\text{s})$  and  $\text{H}(\text{s})$  as well as the bulk gas species of  $\text{CO}$  and  $\text{CO}_2$ . Among these species, the surface adsorbates  $\text{CH}(\text{s})$ ,  $\text{CO}_2(\text{s})$  and  $\text{H}_2\text{O}(\text{s})$  show relatively high sensitivities to the variation of  $\text{H}_2\text{O}$  content. It is interesting to see that the adsorbed species carbon  $\text{C}(\text{s})$  is very sensitive to the variation of  $\text{H}_2\text{O}$  content in the anode, increasing the  $\text{H}_2\text{O}$  content may significantly reduce the adsorbed surface carbon  $\text{C}(\text{s})$ . The high sensitivity of surface adsorbate  $\text{C}(\text{s})$  to  $\text{CH}_4$  and  $\text{H}_2\text{O}$  suggests that suitable combination of  $\text{CH}_4$  and  $\text{H}_2\text{O}$  contents in the anode may mitigate the carbon deposition on the surface of Ni catalyst.

The sensitivities of the bulk gas species and surface adsorbates to the variations of the  $\text{CO}$  and  $\text{CO}_2$  contents in the anode are also studied. The results are illustrated in Fig. 9. When 10% more  $\text{CO}$  is

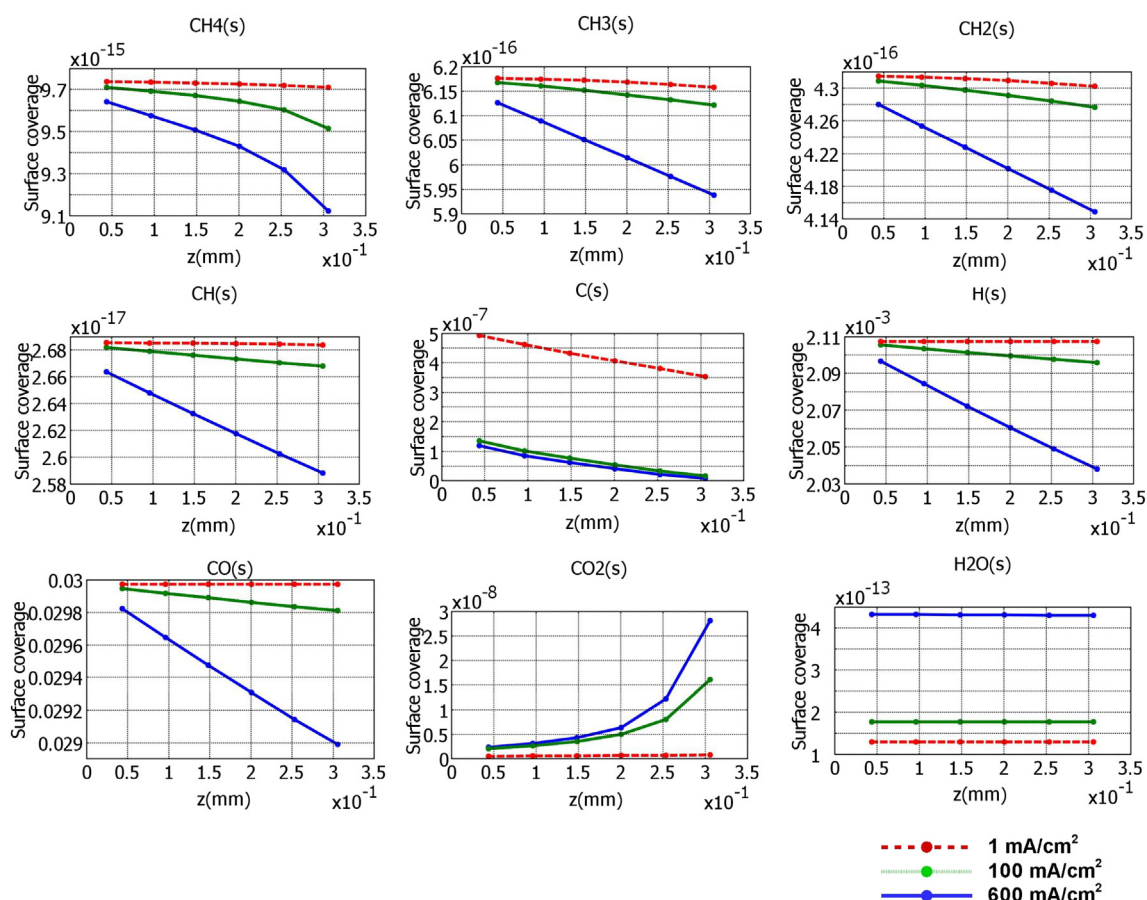


Fig. 7. Distributions of adsorbed species along the axis-symmetrical line of the cell under different cell current loads.



added to the supplied fuel gas, the surface adsorbed carbon C(s) increases significantly, indicating that increasing CO content may potentially intensify the carbon deposition effect. The concentrations of species  $\text{CO}_2$ ,  $\text{CH}_3(\text{s})$ ,  $\text{CH}_2(\text{s})$ ,  $\text{CH}(\text{s})$ ,  $\text{CO}(\text{s})$  and  $\text{H}_2\text{O}(\text{s})$  show different degree of sensitivities and increase with increasing the CO content in the anode. When the  $\text{CO}_2$  content increases, the bulk gas species are not affected; the surface adsorbed species show different sensitivities, including  $\text{CH}_4(\text{s})$ ,  $\text{CH}_3(\text{s})$ ,  $\text{CH}_2(\text{s})$ ,  $\text{CH}(\text{s})$ ,  $\text{H}(\text{s})$ ,  $\text{C}(\text{s})$ ,  $\text{CO}(\text{s})$ ,  $\text{CO}_2(\text{s})$  and  $\text{H}_2\text{O}(\text{s})$ , among which C(s), CH(s), and  $\text{CO}_2(\text{s})$  show relatively high sensitivities to  $\text{CO}_2$  variation.

### 5.5. Effect of surface exchange current density

Theoretically, the surface exchange current is the ongoing current of a redox reaction in both cathodic and anodic directions, which reflects the intrinsic rates of electrochemical processes. The surface exchange current density depends critically on the nature of the electrodes, such as physical structure and electrochemical properties. Since the surface exchange current density has great influence on the cell performance, the sensitivities of bulk gas species and surface adsorbates to the anode and cathode exchange current densities are studied in this section. In particular the exchange current densities are reduced from the base value to the 10% of its base value for the anode ( $i_{\text{an}}$ ) and cathode ( $i_{\text{ca}}$ ) respectively. The corresponding concentration variations of bulk gas species and surface adsorbates are calculated. Here the operating temperature is 700 °C and the cell voltage is set at 0.5 V. As shown in Fig. 10, when the anodic exchange current density reduces to its 10% base value ( $0.1 i_{\text{an}}$ ), the bulk gas species  $\text{H}_2\text{O}$ , CO and  $\text{CO}_2$  decrease, the surface adsorbates  $\text{H}_2\text{O}(\text{s})$  and particularly  $\text{CO}_2(\text{s})$  also show significant decrease. Other surface adsorbates, e.g.,  $\text{CH}_4(\text{s})$ ,  $\text{CH}_3(\text{s})$ ,  $\text{CH}_2(\text{s})$ ,  $\text{CH}(\text{s})$ , C(s), H(s), and CO(s) show different degree of increase with species  $\text{CH}_4(\text{s})$ , C(s), H(s), and CO(s) having relatively high sensitivities. When the cathodic exchange current density reduces to its 10% base value ( $0.1 i_{\text{ca}}$ ), the surface adsorbates  $\text{CO}_2(\text{s})$  and  $\text{H}_2\text{O}(\text{s})$  decrease significantly while the surface adsorbed carbon

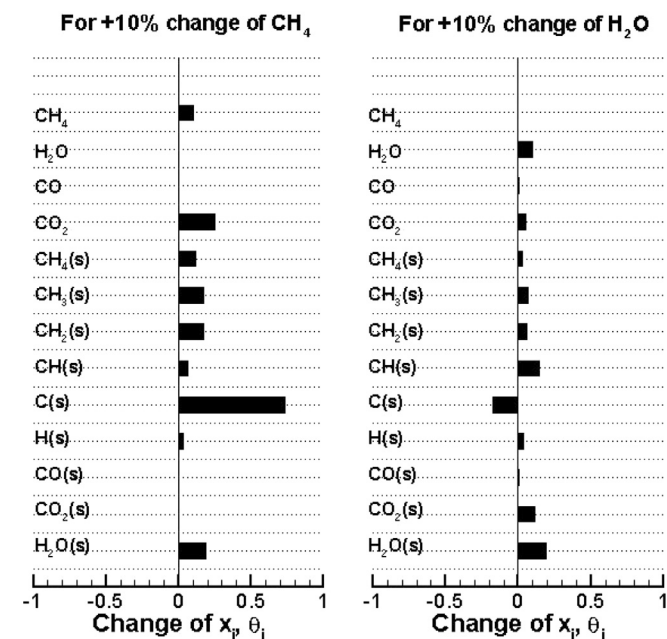


Fig. 8. Sensitivity of 10% increase of the supplied  $\text{CH}_4$  and  $\text{H}_2\text{O}$  on the molar fraction of species and the surface coverage of adsorbed species. The results are obtained at the intersect point between the anode/electrolyte interface and the axial-symmetric line of the cell.

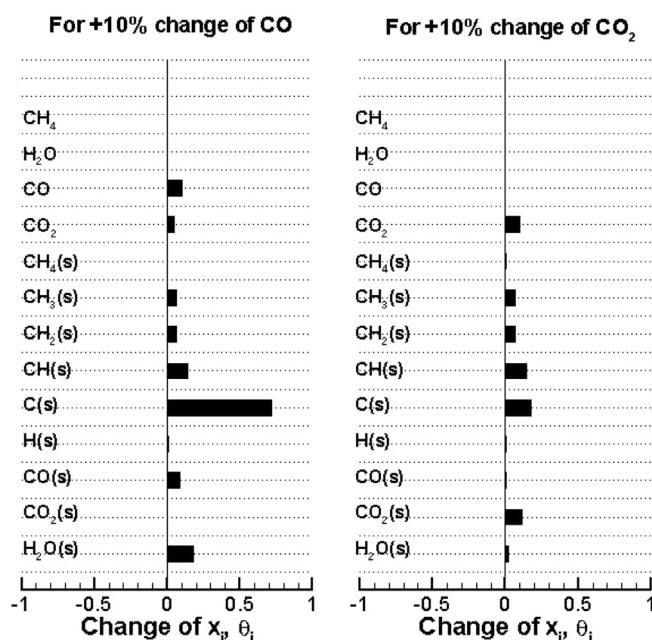


Fig. 9. Sensitivity of 10% increase of the supplied CO and  $\text{CO}_2$  on the molar fraction of species and the surface coverage of adsorbed species. The results are obtained at the intersect point between the anode/electrolyte interface and the axial-symmetric line of the cell.

C(s) increases. The oxygen ions transport from the cathode side to the anode side, where ions react with the adsorbed species H(s), C(s) and CO(s), generating  $\text{CO}_2(\text{s})$  and  $\text{H}_2\text{O}(\text{s})$ . Because the cathodic exchange current density decreases, the number of oxygen ions transported to the anode side also decreases, leading to the above observed surface species variations. Other species including the bulk gas species CO,  $\text{CO}_2$  and the surface adsorbates  $\text{CH}_4(\text{s})$ ,  $\text{CH}_3(\text{s})$ ,  $\text{CH}_2(\text{s})$  show relatively low sensitivities to the variation of cathodic

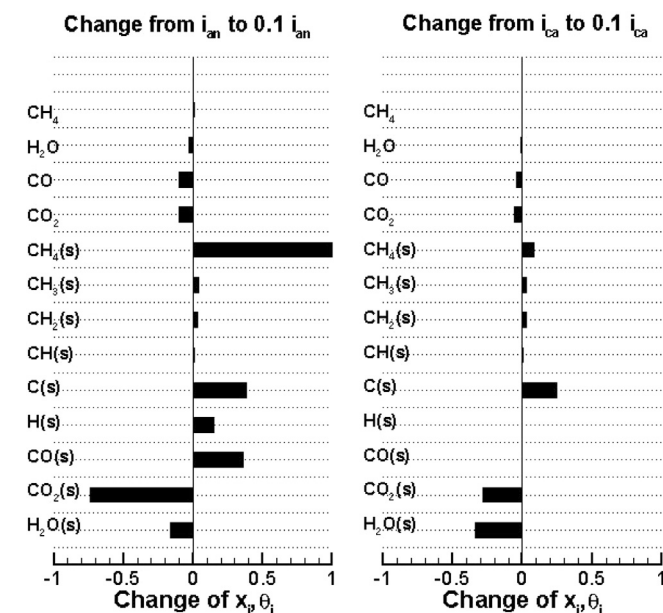


Fig. 10. Effects of the exchange current density of both anode and cathode electrodes on the species molar fraction and the adsorbates surface coverage. The results are obtained at the intersect point between the anode/electrolyte interface and the axial-symmetric line of the cell.

exchange current density. The results also show that surface adsorbed carbon C(s) is very sensitive to the variations of both anode and cathode exchange current density. Thus it facilitates to mitigate the surface carbon deposition by developing high performance electrode materials.

## 6. Conclusion

A comprehensive direct methane-fueled SOFC model is developed based on a physical button cell test system. Both H<sub>2</sub>–H<sub>2</sub>O and CO–CO<sub>2</sub> electro-oxidation processes are considered and coherently integrated into the multi-transport processes of charge, mass, momentum, and energy with the detailed surface reaction processes. The model is validated using the experimental data under the temperatures of 600 °C, 650 °C and 700 °C respectively. Based upon the model validation, extensive simulations are performed to identify complicated transport interactions with the emphasis on surface reaction processes and surface adsorbates. Results show that the surface reactions of methane and electrochemical reactions are relatively intensive near the anode/electrolyte interface. The bulk gas species and surface adsorbates show different degree of sensitivities to operating conditions and electrode properties. The surface adsorbed carbon species is very sensitive to the exchange current density of anode and cathode electrodes and the fuel compositions including CH<sub>4</sub>, H<sub>2</sub>O, CO, CO<sub>2</sub>. To mitigate potential surface carbon deposition, one may: (1) suitably increase H<sub>2</sub>O content in the fuel; (2) reduce the content of CH<sub>4</sub>, CO, CO<sub>2</sub> in the supplied fuel; (3) increase the operating temperature; (4) increase the cell operating current; (5) improve exchange current density of anode and/or cathode electrode by using high performance electrode materials.

## Acknowledgments

The authors gratefully acknowledge the National Science Foundation (grant no. CMMI-1100085, CMMI-1000068), the U.S. DOE Basic Energy Science (grant no. DE-SC0001061), and the University of South Carolina, Office of Research and Graduate Education for financial support.

## Nomenclature

$A$	the Arrhenius parameter for the rate constants
$c_i$	concentration (mol m <sup>-3</sup> )
$D_{m,k}$	ordinary diffusion coefficient (m <sup>2</sup> s <sup>-1</sup> )
$D_{Kn}^{eff}$	Knudsen diffusion coefficient (m <sup>2</sup> s <sup>-1</sup> )
$D_{surf}^{eff}$	surface diffusivity of specie $i$ (m <sup>2</sup> s <sup>-1</sup> )
$D_t^I$	thermal diffusion coefficient (kg m <sup>-1</sup> s <sup>-1</sup> )
$E^0$	the standard potential (V)
$E^{act}$	the thermal activation energy (kJ mol <sup>-1</sup> )
$F$	Faraday's constant (96,485 C mol <sup>-1</sup> )
$G$	the Gibbs free energy (J)
$i_F$	Faradic current density (A m <sup>-2</sup> )
$k_f, k_b$	the forward and backward reaction rate coefficients
$K$	permeability
$K_{eq}$	the equivalent thermal conductivity (W m <sup>-1</sup> K <sup>-1</sup> )
$M_i$	molecular weight of species $i$
$m, n$	the stoichiometric coefficients
$p_i$	the partial pressure of specie $i$
$Q_H$	the heat source term (J mol <sup>-1</sup> )
$r_i$	the rate of elementary reaction $i$
$R$	universal gas constant (8.314 J K <sup>-1</sup> mol <sup>-1</sup> )
$R_i$	mass conservation source term of species $i$

$R_n$	the net reaction rate
$l_{TPB}$	three phase boundary length per unit volume (m m <sup>-3</sup> )
$T$	temperature (K)
$V$	cell voltage (V)
$x_i$	molar fraction of specie $i$
$z$	the number of electrons
$\Gamma$	the available surface site density (mol cm <sup>-2</sup> )
$\eta_{act}$	the activation overpotential (V)
$\theta_i$	surface coverage of adsorbed specie $i$
$\rho$	density (kg m <sup>-3</sup> )
$\sigma_{e,i}$	electronic/ionic charge conductivity (S m <sup>-1</sup> )
$\sigma_i^{surf}$	the number of surface sites occupied by specie $i$
$w_i$	mass fraction of species $i$
$\mu$	viscosity
$\varepsilon$	porosity
$\tau$	tortuosity

## Subscripts

An	anode
Ca	cathode
El	electrolyte
Cl	channel
eff	effective
ohm	ohmic
chem	electrochemical/chemical

## References

- [1] A. Kirubakaran, S. Jain, R.K. Nema, Renewable and Sustainable Energy Reviews 13 (2009) 2430–2440.
- [2] X.W. Zhang, S.H. Chan, G. Li, H.K. Ho, J. Li, Z. Feng, Journal of Power Sources 195 (2010) 685–702.
- [3] Y. Zhu, W. Cai, Y. Li, C. Wen, Journal of Power Sources 185 (2008) 1122–1130.
- [4] V. Liso, A.C. Olesen, M.P. Nielsen, S.K. Kar, Energy 36 (2011) 4216–4226.
- [5] M. Liu, A. Lanzini, W. Halliop, V.R.M. Cobas, A.H.M. Verkooijen, P.V. Aravind, International Journal of Hydrogen Energy 38 (2013) 2868–2883.
- [6] T. Kim, G. Liu, M. Boaro, S.-I. Lee, J.M. Vohs, R.J. Gorte, O.H. Al-Madhi, B.O. Dabbousi, Journal of Power Sources 155 (2006) 231–238.
- [7] N. Akhtar, S.P. Decent, K. Kendall, Journal of Power Sources 195 (2010) 7796–7807.
- [8] H. Paradis, M. Andersson, J. Yuan, B. Sundén, Journal of Fuel Cell Science and Technology 8 (2011) 1–8.
- [9] J. Park, S. Lee, S. Kim, J. Bae, Journal of Fuel Cell Science and Technology 7 (2010) 1–7.
- [10] W.G. Bessler, M. Vogler, H. Stormer, D. Gerthsen, A. Utz, A. Weber, E. Ivers-Tiffée, Physical Chemistry Chemical Physics 12 (2010) 13888–13903.
- [11] W.G. Bessler, S. Gewies, M. Vogler, Electrochimica Acta 53 (2007) 1782–1800.
- [12] M. Vogler, A. Bieberle-Hutter, L. Gauckler, J. Warnatz, W.G. Bessler, Journal of the Electrochemical Society 156 (6) (2009) B663–B672.
- [13] V. Yurkiv, D. Starukhin, H.-R. Volpp, W.G. Bessler, Journal of the Electrochemical Society 158 (1) (2011) B5–B10.
- [14] N.E. McGuire, N.P. Sullivan, O. Deutschmann, H.Y. Zhu, R.J. Kee, Applied Catalysis A: General 394 (2011) 257–265.
- [15] H.Y. Zhu, R.J. Kee, V.M. Janardhanan, O. Deutschmann, D.G. Goodwin, Journal of the Electrochemical Society 152 (2005) A2427.
- [16] V.M. Janardhanan, O. Deutschmann, Journal of Power Sources 162 (2006) 1192–1202.
- [17] G.M. Goldin, H. Zhu, R.J. Kee, D. Bierschenk, S.A. Barnett, Journal of Power Sources 187 (2009) 123–135.
- [18] E.S. Hecht, G.K. Gupta, H.Y. Zhu, A.M. Dean, R.J. Kee, L. Maier, O. Deutschmann, Applied Catalysis A: General 295 (2005) 40–51.
- [19] N. Laosiripojana, S. Assabumrungrat, Journal of Power Sources 163 (2007) 943–951.
- [20] Y. Yang, X. Du, L. Yang, Y. Huang, H. Xian, Applied Thermal Engineering 29 (2009) 1106–1113.
- [21] R.J. Kee, M.E. Coltrin, P. Glarborg, Chemically Reacting Flow. Theory and Practice, John Wiley & Sons, 2003.
- [22] A.S. Loselevich, A.A. Kornyshev, Fuel Cells 1 (2001) 40–46.
- [23] Y. Matsuzaki, I. Yasuda, Journal of Electrochemical Society 147 (2000) 1630–1635.
- [24] Luai Andreassi, Claudia Toro, Stefano Ubertini, Journal of Fuel Cell Science and Technology 6 (2009) 1–15.
- [25] Y. Xie, X. Xue, Solid State Ionics 224 (2012) 64–73.